

Differential Structural Features of Two Mutant ADAR1p150 Zα Domains Associated with Aicardi-Goutières Syndrome

Conner J. Langeberg ¹, Parker J. Nichols ¹, Morkos A. Henen ^{1,2}, Quentin Vicens ^{1,3*} and Beat Vögeli ^{1,3*}

- 1 Department of Biochemistry and Molecular Genetics and RNA Bioscience Initiative, University of Colorado Denver School of Medicine, Aurora, CO 80045, USA
- 2 Faculty of Pharmacy, Mansoura University, Mansoura 35516, Egypt
- 3 RNA Bioscience Initiative, University of Colorado Denver School of Medicine, Aurora, CO 80045, USA

Correspondence to Quentin Vicens and Beat Vögeli: CONNER.LANGEBERG@CUANSCHUTZ.EDU (C.J. Langeberg), PARKER.NICHOLS@CUANSCHUTZ.EDU (P.J. Nichols), MORKOS.HENEN@CUANSCHUTZ.EDU (M.A. Henen), QUENTIN.VICENS@CUANSCHUTZ.EDU (Q. Vicens), BEAT.VOGELI@CUANSCHUTZ.EDU (B. Vögeli)@morkos_henen ♥ (M.A. Henen), @qvicens ♥ (Q. Vicens), @LabVogeli ♥ (B. Vögeli) https://doi.org/10.1016/j.jmb.2023.168040

Edited by Moshe Yaniv

Abstract

The $Z\alpha$ domain of ADARp150 is critical for proper Z-RNA substrate binding and is a key factor in the type-l interferon response pathway. Two point-mutations in this domain (N173S and P193A), which cause neurodegenerative disorders, are linked to decreased A-to-I editing in disease models. To understand this phenomenon at the molecular level, we biophysically and structurally characterized these two mutated domains, revealing that they bind Z-RNA with a decreased affinity. Less efficient binding to Z-RNA can be explained by structural changes in beta-wing, part of the Z-RNA-protein interface, and alteration of conformational dynamics of the proteins.

© 2023 Elsevier Ltd. All rights reserved.

Main

well-functioning immune svstem distinguish non-self from self RNA. This task is in part carried out by the adenosine deaminase acting on RNA (ADAR1), which catalyzes the conversion of some adenosines in self RNA to inosines. 1-3 In humans, this 'A-to-I' editing is augmented upon infection, primarily through the interferon-induced longer isoform of ADAR1 (p150). 1,2 p150 contains a \sim 65-amino acid long Z-RNA binding domain ($Z\alpha$) at its N-terminus (Figure 1 (A)). Zα enhances substrate specificity and enzymatic activity in vitro,3 and acts synergistically with the downstream $Z\beta$ domain.^{4,5} The mechanism that enables ADAR1p150 to achieve this level of specificity in vivo remains unknown.

Inheritable mutations within $Z\alpha$ highlight its importance for self-RNA editing. In particular, the point mutants Asn173Ser $(Z\alpha_{N173S})$ Pro193Ala $(Z\alpha_{P193A})$ decrease editing levels, causing autoimmune diseases. Both mutations are frequently found in patients suffering from Aicardi-Goutières syndrome (AGS) and Bilateral Striatal Necrosis/Dystonia (BSN). 7,9,10 AGS is a Mendelian genetic disorder primarily affecting the nervous system in children, leading to continual activation of the innate immunity response in the absence of a viral infection. 1,7,11 BSN is an earlyonset disease characterized by developmental regression, dystonia, and cerebral calcification.8 Currently, therapies to treat AGS and BSN are of limited efficacy, 11,12 although small-molecule modulators could be therapeutically useful. 13

The P193A ADAR1p150 mutant results in decreased A-to-I editing as measured through transcriptome sequencing, 6 likely due to decreased affinity for substrate dsRNA. Similar studies have not been undertaken for the $Z\alpha_{N173S}$ mutant, though the effects are likely analogous. Because N173 and P193 in Za are involved in the recognition of Z-form nucleic acids, 14,15 we sought to investigate the effect of the AGS- and BSN-related N173S and P193A mutations on the three-dimensional structure of the $Z\alpha$ domain and its ability to bind RNA, the former a critical binding residue while the latter is involved in binding as well as the conversion to Z-form. 16 Therefore, we aimed to understand structurally if this loss of binding was simply a result of the loss of key binding residues or if there are unforeseen consequences of these mutations.

Previous in vivo analyses of AGS-causing mutants ADAR1 isoforms suggest many of the identified mutations within the binding domains result in a decrease or loss of binding affinity to substrate dsRNA, 17 though many of these mutants lack robust biophysical or biochemical characterization. However, limited biophysical data has shown a loss or decrease in binding as measured by CD or NMR of the $Z\alpha$ double mutant N173A, Y177A¹⁸ as well as K169A, K170A, and R174A¹⁹ mutants. Because studies of N173A (not the clinically observed mutation) and P193A suggest a perturbation to Z-form RNA binding as the means by which these two mutants result in disease, we sought to biophysically characterize dsRNA binding to $Z\alpha_{N173S}$ and $Z\alpha_{P193A}$. Circular dichroism (CD) provides a spectral evaluation of A-form and Z-form character of RNA. We used this method to evaluate the ability of $Z\alpha$ to induce the conversion from Aform unbound RNA to bound Z-form. Using CD, we are also able to discriminate the ability of the mutant Zα domains to bind an idealized substrate dsRNA. By measuring the CD spectra of an RNA hexamer (CpG)₃ dimer in the presence of $Z\alpha_{WT}$ or the mutants, we determined that $Z\alpha_{WT}$ can induce Z-form, as noted by a decrease in the peak at 266 nm, the presence of a peak at 285 nm, and the 295 nm peak changing from negative to positive. However, neither of the mutants were able to induce Z-form in the RNA, retaining their characteristic A-form peaks (Figure 1(B)).

As an orthogonal method to quantitatively probe the mutant $Z\alpha$ domains' dsRNA binding, we used isothermal titration calorimetry (ITC) to determine binding affinities for $Z\alpha_{WT}$ and the two AGS mutants. $Z\alpha_{WT}$, when challenged with a (CpG)₃ homodimer, yielded a K_d of 240 nM with a stoichiometry of 0.4 (Figure 1(C)), indicating the binding of two $Z\alpha$ proteins per (CpG)₃ dimer (as observed in the crystal structure ¹⁴). Conversely, both mutants demonstrated increased K_d values, thus decreased substrate affinity, 3.1 μ M for $Z\alpha_{N173S}$ and 2.4 μ M for $Z\alpha_{P193A}$ with stoichiometries of 0.7 and 0.9 respectively (Figure 1(C)). This

observed decrease in substrate affinity is consistent with the CD measurements and potentially explains the decreased A-to-I editing observed in $Z\alpha_{P193A}$ of ADAR1p150,6 as well as suggesting a decrease in editing would also be observed for $Z\alpha_{N173S}$. Because the mutations causing this decreased affinity occur outside of the catalytic deaminase domain, we speculate that while the k_{cat} may be unchanged, the weaker binding affinity mandates a faster k_{off} , slower k_{on} , or a combination. The result of this would be relatively elevated K_M and decreased catalytic efficiency, though further experiments are needed to confirm this. Interestingly, while both $Z\alpha_{WT}$ and $Z\alpha_{N173S}$ demonstrated negative -T Δ S terms, the Z α_{P193A} mutant yielded a positive term. This may reflect an increase of microstates that Z_{2P193A} may occupy, though additional work is required to confirm this.

We then purified human 15 N/ 13 C-labeled proteins from *Escherichia coli* and characterized them by NMR. Chemical shift perturbations (CSP) derived from the Z α mutants in reference to the wild type spectrum reveal two different patterns of perturbations. While chemical shifts within $Z\alpha_{N173S}$ are distributed throughout the domain, for $Z\alpha_{P193A}$ they localize to the mutation-containing binding loop and the N-terminal region of helix 2 (Figure 2 (A), S1, S2).

To better assess local single residue and global alterations of protein dynamics for the $Z\alpha_{N173S}$ and measured $Z\alpha_{P193A}$, we NMR relaxation experiments sensitive to different time scales. Both local and global dynamics can be assessed by various NMR relaxation experiments at various timescales. Picosecond to nanosecond dynamics can be probed by R₁ and cross-correlation relaxation (CCR) experiments, while us to ms dynamics, often indicative of domain motion, are probed by R_{1p} relaxation experiments. The average ¹⁵N-R₁ relaxation rate was essentially unaltered between the two Z α mutants (1.7 s⁻¹ for $Z\alpha_{N173S}$; 1.6 s⁻¹ for $Z\alpha_{P193A}$), compared to $Z\alpha_{WT}$ (1.5 s⁻¹; Figure S3). ¹⁵N CSA/¹H-¹⁵N dipole CCR is also similar for the two mutants (4.8 s^{-1}) and 3.8 s⁻¹ for $Z\alpha_{N173S}$ and $Z\alpha_{P193A}$, respectively; Figure S4). Because both R₁ and CCR probe molecular tumbling on the fast timescale (ps to ns), these data imply little change to molecular tumbling. However, average R₁₀ relaxation rates that are also sensitive to µs to low ms dynamics, were faster than expected for $Z\alpha_{N173S}$ (11.4 s⁻¹) than for $Z\alpha_{P193A}$ (7.8 s⁻¹), which is similar to $Z\alpha_{WT}$ (7.6 s⁻¹; Figure S4, S5). Based on the slightly elevated R_1 and CCR values for $Z\alpha_{N173S}$, only half of the difference in the $R_{1\rho}$ relaxation rates can be explained by dynamics faster than \sim 10 ns. In support of these findings, analytical ultracentrifugation and size exclusion experiments yielded results consistent with a monomeric state, thus excluding the possibility of substantial dimerization (data not shown). Comparing the

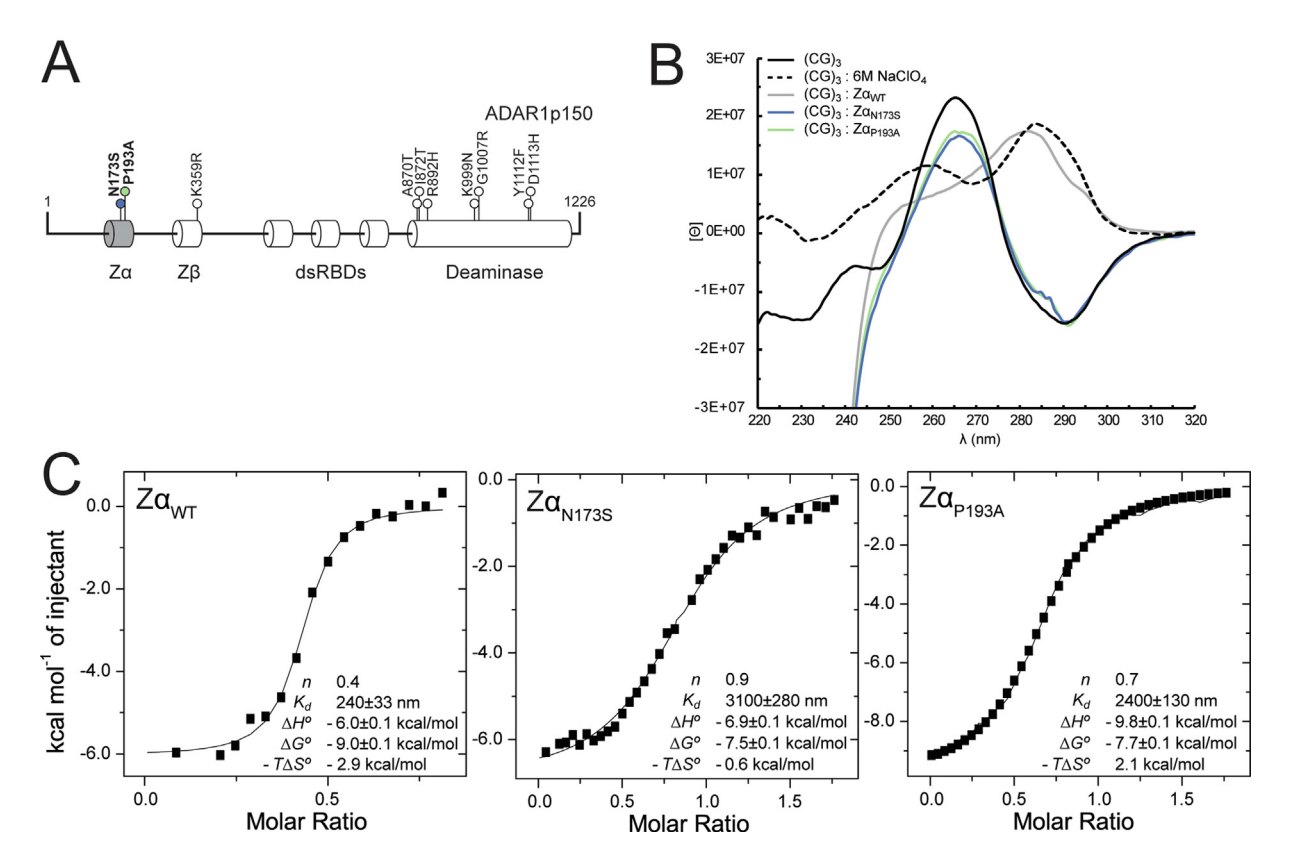


Figure 1. Both AGS mutants of $Z\alpha$ have decreased binding affinity for substrate dsRNA and fail to convert it to the Z-form. (A) Domain schematic of human ADAR1p150 showing known AGS associated mutations⁷ (B) Circular dichroism spectra of a $(CpG)_3$ dimer in the presence and absence of wild type and mutant $Z\alpha$. NaClO₄ is used to have a reference Z-form. (C) Binding isotherms derived from ITC of $(CpG)_3$ dimer and wild type or mutant $Z\alpha$ and extracted biophysical values.

dynamic trends for residue 173 shows similar $^{15}\text{N-R}_1$ values (1.6 for N173; 1.7 for S173; Figure S3) while the $^{15}\text{N-R1}_\rho$ value was elevated for S173 (9.2 for N173; 14.0 for S173; Figure S5). This disparity between the $Z\alpha_{WT}$ domain and $Z\alpha_{N173S}$ is a reflection of altered global dynamics of $Z\alpha_{N173S}$, arising from a single solvent facing residue. Overall, our findings suggest that $Z\alpha_{P193A}$ has similar dynamics to $Z\alpha_{WT}$, while $Z\alpha_{N173S}$ has altered domain dynamics.

To gain further insight, we calculated the complete structure of the mutant $Z\alpha$ domains using exact NOEs (eNOE) derived from NOESY spectra (Figure 2(B,C), S6). This recently described method nakes use of NOESY spectra with increasingly longer mixing times to extract high precision proton pair distances to yield precise structures. In accordance with the CSP and relaxation data, $Z\alpha_{P193A}$ demonstrates overall minimal deviation from $Z\alpha_{WT}$ (heavy atom RMSD = 1.1 Å). Similarly, $Z\alpha_{N173S}$ overlays well with $Z\alpha_{WT}$ (heavy atom RMSD = 1.3 Å) as compared to the structure of the $Z\alpha_{N173A,Y197A}$ double mutant relative to $Z\alpha_{WT}$ (heavy atom RMSD = 0.6 Å).

In $Z\alpha_{P193A}$, the binding loop containing the point mutation undergoes a structural displacement of 5.8 Å away at its apex from its position in $Z\alpha_{WT}$ (Figure 2(C)), similar to MD simulations of this mutant. An overlay with dsRNA-bound $Z\alpha_{WT}$ reveals that this loop reorganization displaces several nucleic acid binding residues from the RNA binding interface which normally make key hydrogen bonding and Van der Waals contacts with Z-RNA and Z-DNA, specifically; Trp191, Pro192, Pro193, and Trp195. Similarly, the structural disruption of the beta-wing likely compounds the mutant's failure to properly bind substrate. This disruption of the beta-wing also likely impacts proper Z-form conversion as this motif has been shown to be important for this role in other $Z\alpha$ domains. 16

Although $Z\alpha_{N173S}$ overlays with the $Z\alpha_{WT}$ crystal structure, one feature of note is a minor perturbation in the beta-wing which shows small structural perturbations from the known crystal structure (backbone RMSD 1.9 Å) (Figure 2(B), S7). This is interesting, as the structure ensemble for the $Z\alpha_{N173A,Y197A}$ double mutant shows similar displacements, ¹⁸ suggesting that mutations within

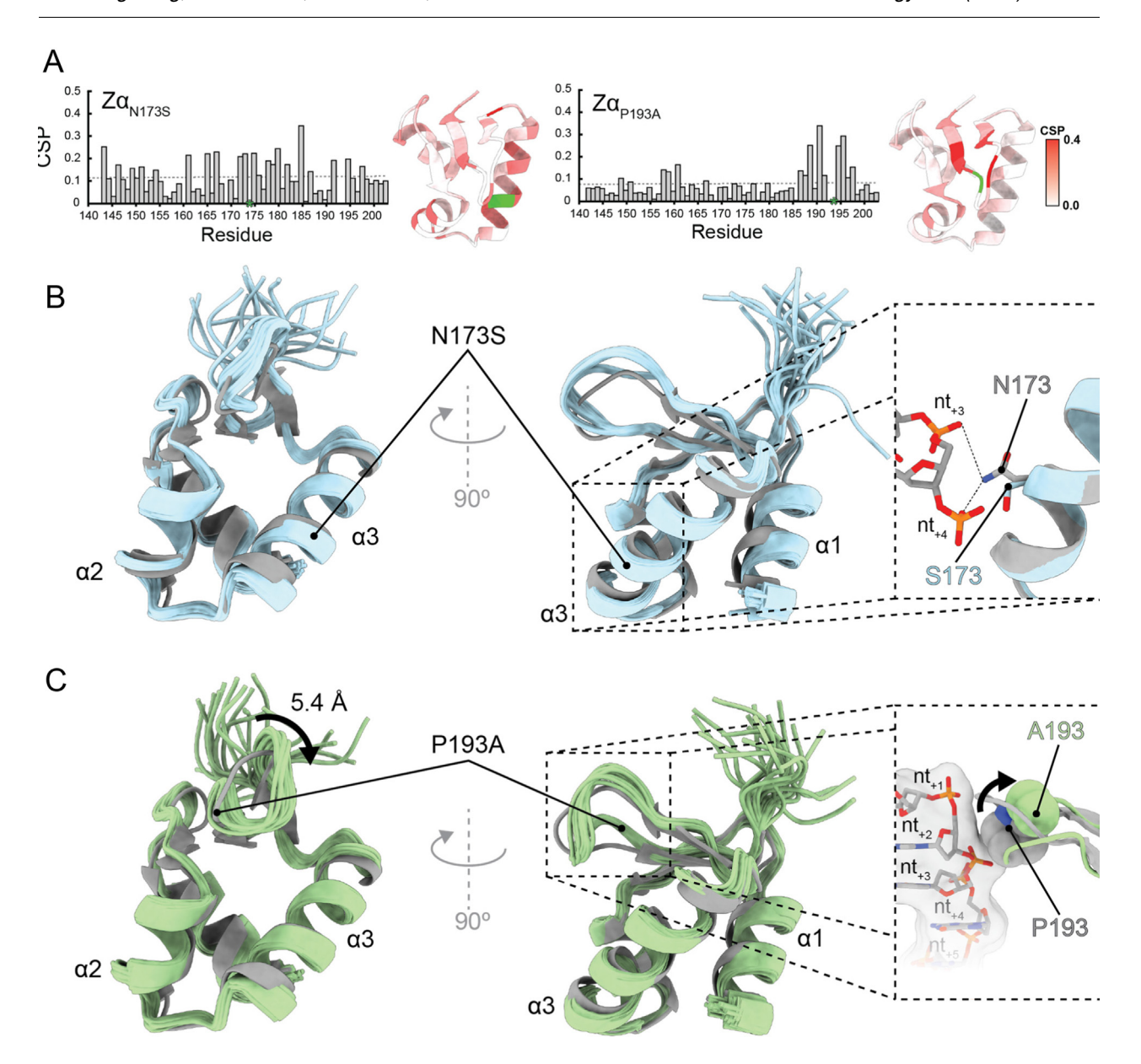


Figure 2. The structures of two Aicardi-Goutières Syndrome mutants of the ADARp150 $Z\alpha$ domain. (A) Chemical shift perturbations (CSP) of both AGS mutants of the $Z\alpha$ domain in reference to the wild type mapped onto the crystal structure of $Z\alpha$ (PDB 1QGP²⁸). The site of the mutation is colored in green and the CSP average is denoted with a dashed line. (B) Superposition of the twenty lowest energy structures of $Z\alpha_{N173S}$ and the crystal structure of $Z\alpha$. (C) Superposition of the twenty lowest energy structures of $Z\alpha_{P193A}$ and the crystal structure of $Z\alpha$.

helix 3 may affect beta wing dynamics. However, the loops may also adopt different conformations because the structures are not in complex with Z-form nucleic acids, as reported before for $Z\alpha$ of PKZ. Quite possibly, differences in loop conformations may be due to the more sparce eNOEs observed in this region of the spectra (Figure S6). In any case, our analysis reveals that a loss of contacts at position 173 is not the sole reason why $Z\alpha_{N173S}$ shows decreased binding to RNA. Replacing the asparagine at position 173 with a serine leads to a global perturbation of the domain dynamics while the global structure remains largely unaltered. The observed effect is thus different from

that seen in $Z\alpha_{P193A}$, in which the change of amino acid at position 193 leads to disruption of protein-RNA contacts through the reorganization of the beta-wing motif rather than altered dynamics.

The data presented here provide structural insight into how these AGS mutants potentially result in diseases which have remained poorly understood. In the case of $Z\alpha_{N173S}$, the globally altered dynamics we observe may explain the disease phenotype observed resulting from this mutation. This result expands upon the previous postulate that the loss of function is solely the result of the disruption of a single binding residue. Additionally, our findings reinforce the idea that in some cases

the observed dysfunction of protein resulting from a point mutation cannot be explained by the loss of an important hydrogen bond or ionic interaction, but rather there may be unforeseen consequences of these mutations, as is seen here where structure predictions of the $Z\alpha_{P193A}$ domain fail to recapitulate the local structural perturbation (Figure S8). Our findings serve as a reminder of the work of Brian Matthews, who was among the first to reveal how point mutations within proteins lead to conformation variability.²⁴ Systematically studying the structures of proteins with point mutations causing disorders provides a more robust molecular understanding of the associated dysfunctions, while ultimately also helping to improve our tools for predicting the effect of mutations on protein structures.25

Methods

Expression of unlabeled human ADAR1p150's $Z\alpha$ domain

The $Z\alpha$ domain of hADAR1p150 (residues 140-202) (UniProt ID: P55265) cloned in the pET28a (+) plasmid (N-terminal 6x His-tag and thrombin cleavage site between His-tag and the $Z\alpha$ sequence) was a gift from Drs. Peter Dröge and Alekos Athanasiadis. The $Z\alpha_{N173S}$ and $Z\alpha_{P193A}$ mutants were synthesized and cloned into pET28a(+) vectors by Genscript and confirmed through sequencing. Different $Z\alpha$ constructs were expressed and purified similarly as described in. 4,15 The proteins were recombinantly expressed in BL21(DE3) E.coli cells. Cells were grown in LB to an OD₆₀₀ of 0.6 and then induced with 0.5 mM isopropyl β-D-1-thiogalactopyranoside (IPTG) overnight at 18 °C. After pelleted cells were resuspended in lysis buffer containing 50 mM Tris-HCl (pH 8.0), 300 mM NaCl, 10 mM imidazole, and 5 mM β-mercaptoethanol (BME), they were chemically lysed by deoxycholic acid at 2 mg mL⁻¹ for 30 minutes on ice. The cell lysate was then sonicated for 15 rounds of 15 seconds on, 30 seconds off at 50 W on ice. The cell lysate was clarified by centrifugation at 30,000xg for 30 minutes. The soluble fraction was purified by nickel affinity chromatography (Histrap column) using a wash buffer containing 1 M NaCl, 50 mM Tris (pH 8.0), 10 mM imidazole, and 5 mM β-mercaptoethanol, followed by elution in 300 mM NaCl, 50 mM Tris (pH 8.0), 500 mM imidazole, and 1 mM BME. To further purify the prosize exclusion chromatography was performed using a Sepax 300 SEC column (GE Life Sciences) in 100 mM NaCl and 50 mM sodium phosphate (pH 6.4). Protein stocks were stored at -80 °C.

Expression of ^{13}C and ^{15}N labeled human ADAR1p150's $Z\alpha$ domain

Proteins were prepared as described above with the following modifications to the protocol. Cell growth was carried out in M9 minimal media containing the following components: 100 mL of 10x M9 salts (60 g/L Na₂HPO₄, 30 g/L KH₂PO₄, 5 g/L NaCl, pH 7.4), 10 mL of 100 g/L ¹⁵NH₄Cl (pH 7.4), 2 mL 1 M MgSO₄, 12.5 mL 20% (w/v) ³C-glucose, 0.2 mL 0.5 M CaCl₂, 1 mg biotin, 0.5 mL 2 mg/mL thiamine hydrochloride, 1 mL 15 mg/mL FeCl₂ in 1 M HCl, 1 mL 15 mg/mL ZnCl₂, 2 mL 10% (w/v) yeast extract. The media was brought to 1 L with autoclaved milli-Q filtered water and then passed through a 0.22 µM filter. Cells were grown to an OD₆₀₀ of 0.4 and induced 0.5 isopropyl with mΜ β-D-1thiogalactopyranoside (IPTG) for 3 hours at 37 °C.

Nucleic acid constructs

 $(CpG)_3$ RNA oligo constructs were purchased from Dharmacon.

RNA circular dichroism

All CD experiments were performed at 100 μ M duplex oligo (0.38 mg/mL) and 600 μ M protein (5.4 mg/mL) in a buffer containing 25 mM NaCl and 20 mM sodium phosphate (pH 6.4) unless otherwise indicated. Oligoribonucleotides were briefly heated to 90 °C and cooled to room temperature. Spectra were acquired in a JASCO J-815CD spectrometer using a 1 mm quartz cuvette. Spectra were an average of two scans measured from 320 to 220 nm with a 1 nm step using a scanning speed of 50 nm/min and a digital integration time of 4 seconds. Then protein was added to the indicated concentration and incubated at room temperature for 10 min.

Isothermal titration calorimetry

Nucleic acid oligoribonucleotides and protein for ITC were dialyzed overnight at 4 °C in the same beaker against a buffer containing 25 mM NaCl and 20 mM sodium phosphate (pH 6.4). Binding heat was measured using a Malvern ITC200 calorimeter at 25 °C and mixing speed of 750 RPM, with 180 s injection delays and a reference power of 10 μ cals⁻¹. For $Z\alpha_{WT}$, the titration was measured with twenty 2 µL consecutive injections of 500 μ M r(CpG)₃ RNA into 50 μ M protein. Titrations with $Z\alpha_{N173S}$ and $Z\alpha_{P193A}$ mutants were measured with twenty 2 µL consecutive injections of 500 μM RNA into 50 μM protein followed by an additional twenty 2 µL consecutive injections of 500 μM RNA into the cell and concatenation of the two datasets using MicroCal Concat ITC version 1 (Malvern). All ITC thermograms were analyzed and fit using Microcal Analysis version 7 SR4 (Origin).

AlphaFold2 structure prediction

The sequence of either mutant domain was submitted to the $\operatorname{ColabFold}^{26}$ server running Alpha-

Fold2 for structure prediction. The primary sequence of each mutant domain was input and run using MMseqs2 and AlphaFold2-ptm mode. The top 5 confidence models were returned and the highest scoring model was used for comparison with the experimentally recovered structures.

NMR Spectroscopy

All NMR experiments were carried out on a Varian 900 MHz (run using VNMRJ version 4.2 Revision A (Agilent)) equipped with a 5 mm triple resonance $^1\text{H}/^{13}\text{C}/^{15}\text{N}$ cold probe with a Z-axis gradient and a Bruker 600 MHz spectrometers (run using TopSpin version 7 (Bruker)) equipped with a 5/3 mm triple resonance $^1\text{H}/^{13}\text{C}/^{15}\text{N}/^{19}\text{F}$ cryoprobe (CP2.1 TCI) in 100 mM NaCl and 20 mM potassium phosphate (pH 6.4) with 5% D₂O. For all non-uniformly sampled (NUS) experiments, schedules were generated using Poisson-Gap sampling from Gerhard Wagner's lab website: http://gwagner.med.harvard.edu/intranet/hmsIST/gensched_new.html. 27

Wild-type Z α . The NMR resonance assignment and structure calculation of wild-type Z α have been carried out previously²⁸ and backbone chemical shifts can be found under BMRB accession code 50714.²⁹

The ^{15}N -HSQC spectrum of wild-type $Z\alpha$ was collected on the Varian 900 MHz spectrometer with 1048 (1 H) \times 120 (15 N) complex points, a 2 s recycle delay, 8 scans, and spectral widths of 16 and 35 ppm for the ¹H and ¹⁵N dimensions, respectively. The ¹⁵N CSA/¹⁵N-¹H dipole–dipole cross-correlated relaxation (CCR) experiment³⁰ was run on the Varian 900 MHz spectrometer with $1024 (^{1}H) \times 96 (^{15}N)$ complex points, a 1.7s recycle delay, 20 scans, and spectral widths of 15.6 and 35 ppm for the ¹H and ¹⁵N dimensions, respectively. The effective periods during which CCR was active were 0, 20, 40, 60, 80, 100, 120, and 150 ms. The ¹⁵N R₁ relaxation experiment was collected on the 900 MHz Varian spectrometer and run with 1048 $(^{1}\text{H}) \times 80 \ (^{15}\text{N})$ complex points, a recycle delay of 2 s, 8 scans, and spectral widths of 16 and 35 ppm for the ¹H and ¹⁵N dimensions, respectively. The relaxation delays were 0, 100, 200, 300, 400, 500, 600, 700, 800, and 900 ms. The ¹⁵N R₁₀ relaxation experiment was run with 1048 (1 H) \times 80 (15 N) complex points, a recycle delay of 2 s, 8 scans, and spectral widths of 16 and 35 ppm for the ¹H and ¹⁵N dimensions, respectively. The relaxation delays under a spin-locking field strength of 1500 Hz were 0, 20, 40, 60, 80, 100, 120, 140, 160, and 180 ms.

 $Z\alpha_{N173S}$ mutant. The ¹⁵N-HSQC spectrum of the $Z\alpha_{N173S}$ mutant was collected on the Bruker 600 MHz spectrometer with 1024 (¹H) \times 160 (¹⁵N) complex points, a 1.6 s recycle delay, 32 scans, and spectral widths were 16 and 35 ppm for the

¹H and ¹⁵N dimensions, respectively. The constant time ¹³C-HSQC spectrum was collected on the Bruker 600 MHz spectrometer with 1024 $(^{1}H) \times 128 (^{13}C)$ complex points, a 1.6 s recycle delay, 32 scans, and spectral widths of 16 and 80 ppm for the ¹H and ¹³C dimensions. The [¹⁵N,¹³C]-HNCACB respectively. collected on the Bruker 600 MHz spectrometer with 1024 (1 H) \times 40 (15 N) \times 64 (13 C) complex points (1268 of the total 2560 indirect points were collected following a 50% NUS sampling scheme), a 1 s recycle delay, 16 scans, and spectral widths of 13.6 (¹H), 35 (¹⁵N), and 80 (¹³C) ppm. The ¹⁵N-HBHANH experiment was collected on the Bruker 600 MHz spectrometer with 1024 (1 H) \times 50 $(^{15}N) \times 64$ (^{1}H) complex points (1275 of the total 3200 points were collected following a 40% NUS sampling scheme), a 1 s recycle delay, 16 scans, and spectral widths of 16 (1H), 35 (15N), and 16 (1H) ppm. The [13C]-HCCH TOCSY was collected on the Bruker 600 MHz spectrometer with 1024 $(^{1}H) \times 40 (^{13}C) \times 120 (^{1}H)$ complex points (1905) of the total 4800 points were collected following a 40% NUS sampling scheme), a 1 s recycle delay, 16 scans, and spectral widths of 13.6 (1H), 80 (¹³C), and 13.6 (¹H) ppm. A uniformly-sampled 3D simultaneously [¹⁵N, ¹³C]-resolved [¹H, ¹H,X^{13C,15N}]-NOESY²⁰ was collected on the Varian 900 MHz spectrometer with 1024 (1 H) \times 160 (1 H) \times 50 (X^{13C,15N}) complex points, a recycle delay of 1.2 s, 4 scans, spectral widths of spectral widths 15.6 (¹H), 15.6 (¹H), 34/30 ppm (¹⁵N/¹³C), and a NOESY mixing time of 60 ms. The NUS NOESY buildup series with NOESY mixing times of 20, 30, 40, 50, and 60 ms was collected in the same manner as the uniformly-sampled case but following a 50% NUS sampling scheme (4010 out of the total 8000 points were collected)²¹. The ¹⁵N CSA/15N-1H dipole-dipole cross-correlated relaxation (CCR) experiment³¹ was run on the Varian 900 MHz spectrometer with 1024 $(^{1}H) \times 96 (^{15}N)$ complex points, a 1.7 s recycle delay, 20 scans, and spectral widths of 15.6 and 35 ppm for the ¹H and ¹⁵N dimensions, respectively. The effective periods during which CCR was active were 0, 20, 40, 60, 80, 100, 120, and 150 ms. The ¹⁵N R₁ relaxation experiment was run on the Varian 900 MHz spectrometer with 1048 (1 H) \times 32 (15 N) complex points, a recycle delay of 2 s, 8 scans, spectral widths of 16 and 35 ppm for the ¹H and ¹⁵N dimensions, respectively, and relaxation delays of 0, 100, 200, 300, 400, 500, 600, 700, 800, and 900 ms. The ¹⁵N R_{1p} relaxation experiment was run on the Varian 900 MHz spectrometer with 1048 $(^{1}H) \times 32 (^{15}N)$ complex points, a recycle delay of 2 s, 8 scans, spectral widths of 16 and 35 ppm for the ¹H and ¹⁵N dimensions, respectively, and relaxation delays of 0, 20, 40, 60, 80, 100, 120, 140, 160, and 180 ms under a spin-locking field

strength of 1500 Hz. The $[^{1}H^{-15}N]$ -heteronuclear NOE enhancement experiment was run on the Varian 900 MHz spectrometer with 1024 $(^{1}H) \times 80 (^{15}N)$ complex points, a 1 s recycle delay, 20 scans, and spectral widths of 15.6 and 33 ppm for the ^{1}H and ^{15}N dimensions, respectively. Spectra in the presence and absence of ^{1}H saturation were recorded in an interleaved manner.

 $Z\alpha_{P193A}$ mutant. All experiment run on the $Z\alpha_{P193A}$ mutant were repeated for the $Z\alpha_{P193A}$ mutant. Slightly different parameters were used for the following experiments: The ¹⁵N-HSQC spectrum was collected with 1024 (¹H) \times 94 (¹⁵N) complex points. The [¹⁵N,¹³C]-HNCACB was collected with 1024 (¹H) \times 40 (¹⁵N) \times 44 (¹³C) complex points (937 of the total 1760 points were collected following a 50% NUS sampling scheme). The [¹H-¹⁵N]-heteronuclear NOE enhancement experiment was run with 48 scans, and spectral widths of 16 and 33 ppm for the ¹H and ¹⁵N dimensions, respectively.

Data processing. All spectra were processed with the NMRPipe/NMRDraw/NlinLS package.³¹ The time-domain data were multiplied with a squared cosine function in the direct dimension and cosine functions in the indirect dimensions and the number of complex points were doubled by zero-filling once. A polynomial function was used for solvent suppression. The 3D NUS-spectra were constructed using the hmsIST software.²⁷

Resonance assignment. Resonance assignment was performed using the CCPNmr analysis software version 2.4.2t.³² Chemical shift assignments for the $Z\alpha_{N173S}$ and $Z\alpha_{P193A}$ constructs have been submitted to the Biological Magnetic Resonance Data Bank (BMRB) under entry codes 51833 and 51834, respectively.

Calculation of R_2 and τ_{corr} from R_1 and $R_{1\rho}$. Transverse R_2 relaxation rates were calculated from longitudinal R_1 and spin-locked longitudinal $R_{1\rho}$ relaxation rates using the following equation:

$$R_2 = R_{1\rho} + (R_{1\rho} - R_1) \tan^2(\theta)$$

where $\theta = \tan(\gamma_{\rm N} B_{\rm 1}/2\pi\Delta {\rm v})$, $\Delta {\rm v}$ is the resonance offset, I $\gamma_{\rm N} B_{\rm 1}/2\pi {\rm l}$ is the strength of the spin-lock field B₁, and $\gamma_{\rm N}$ is the gyromagnetic ratio of the ¹⁵N spin. Effective overall tumbling times τ_{corr} were then calculated from the R_2/R_1 ratio.³³

Chemical shift perturbation determination. Chemical shift perturbations were determined between the wild type protein and either mutant protein using the according 1 H- and 15 N-chemical shifts δ in the following equation:

$$\textit{CSP} = \sqrt{\left(\delta_{\textit{H,WT}} - \delta_{\textit{H,mut}}\right)^2 + 0.2\left(\delta_{\textit{N,WT}} - \delta_{\textit{N,mut}}\right)^2}$$

NOESY buildup fitting and extraction of distance restraints

The uniformly-sampled 3D simultaneously $[^{15}N,^{13}C]$ -resolved $[^{1}H,^{1}H,X^{13C,15N}]$ -NOESY 20 spectra measured on $Z\alpha_{N173S}$ and $Z\alpha_{P193A}$ constructs with 60 ms mixing times were assigned in CCPNmr. 32 The peaks were then transferred to the corresponding 60 ms NUS NOESY spectra and peaks which decreased significantly in quality due to NUS²¹ were removed. The peak lists were then exported to NMRPipe format, and then crossand diagonal-peak intensities at all mixing times (20, 30, 40, 50, and 60 ms mixing times) were extracted using the NlinLS autofit script in NMRPipe. Fitted auto-relaxation rate constant (ρ) and initial magnetization (Mo) values were used to determine cross-relaxation rate constants (σ) using the full-matrix approach³⁴ package implemented in CYANA³⁵ version 3.98. Spin-diffusion corrections were calculated using the previously solved NMR structure of the wild-type $Z\alpha$ from *H. sapiens* ADAR1p150 (PDB ID: 1QGP²⁸) and applied to the intensities of the cross-peak buildup curves. We used the average *tcorr* values calculated from R₂/ R_1 of the respective $Z\alpha_{N173S}$ and $Z\alpha_{P193A}$ constructs as inputs for the spin-diffusion corrections. The quality of the fits was inspected visually, and subpar buildups were discarded. Previously determined error tolerances for bi- and uni-directional eNOEs³⁶ were automatically applied by CYANA.

Structure calculations

Structure calculations of the $Z\alpha$ constructs were carried out in CYANA 3.9835 using 275 bidirectional eNOEs, and 489 uni-directional eNOEs as input for $Z\alpha_{P193A}$ and 198 bi-direcitonal eNOEs, and 513 uni-directional eNOEs as input for $Z\alpha_{N173S}$. The calculations started with 100 initial structures with random torsion angle values using the standard simulated annealing protocol with 50,000 torsion angle dynamics steps. The 20 structures with the lowest target function values were selected for the ensembles. Distance restraints causing violations larger than 1 Å were discarded and the structures were re-calculated. Backbone RMSD values of the two constructs are reported for all residues excluding the flexible termini (resides: 140-198). The final structures of $Z\alpha_{N173S}$ and $Z\alpha_{P193A}$ were deposited in the Protein Data Bank with codes 8GBC and 8GBD, respectively.

CRediT authorship contribution statement

Conner J. Langeberg: Conceptualization, Investigation. Parker J. Nichols: Conceptualization, Investigation. Morkos A. Henen: Conceptualization, Investigation, Supervision. Quentin Vicens: Conceptualization, Supervision, Funding acquisition. Beat Vögeli:

Conceptualization, Supervision, Funding acquisition.

DATA AVAILABILITY

Data will be made available on request.

Acknowledgements

The authors thank Jeff Kieft for support: current and former Kieft Lab and Vögeli Lab members for thoughtful discussions and technical assistance: and the Biophysics core and NMR facilities at the of Colorado, University Anschutz Medical Campus. This research is funded by NSF grant 1917254 for Infrastructure Innovation for Biological Research and a start-up package from the University of Colorado to B.V., University of Colorado Cancer Center Support Grant P30 CA046934, NIH grant S10OD025020 for shared instrumentation, high-end R35GM118070, NIH grant 1F31Al167396-01 to P. N., NIH grant 1R21 Al171827 to M.A.H. and NSF grant 2153787 to B.V. and Q.V.

Declaration of Competing Interest

The authors declare that they have no known competing financial interests or personal relationships that could have appeared to influence the work reported in this paper.

Appendix A. Supplementary data

Supplementary data to this article can be found online at https://doi.org/10.1016/j.jmb.2023. 168040.

Received 9 January 2023; Accepted 28 February 2023; Available online 7 March 2023

Keywords:

Aicardi-Goutières syndrome; ADAR1; Biophysics; RNA recognition; Z-RNA

References

- Chung, H. et al, (2018). Human ADAR1 Prevents Endogenous RNA from Triggering Translational Shutdown. Cell 172, 811–824.e14.
- Nakahama, T., Kawahara, Y., (2021). Deciphering the biological significance of adar1-z-rna interactions. *Int. J. Mol. Sci.* 22, 1–14.

- Koeris, M., Funke, L., Shrestha, J., Rich, A., Maas, S., (2005). Modulation of ADAR1 editing activity by Z-RNA in vitro. *Nucleic Acids Res.* 33, 5362–5370.
- Schwartz, T. et al, (1999). Proteolytic dissection of Zab, the Z-DNA-binding domain of human ADAR1. *J. Biol. Chem.* 274, 2899–2906.
- Athanasiadis, A., (2012). Zalpha-domains: At the intersection between RNA editing and innate immunity. Semin. Cell Dev. Biol. 23, 275–280.
- Mannion, N.M. et al, (2014). The RNA-Editing Enzyme ADAR1 Controls Innate Immune Responses to RNA. Cell Rep. 9, 1482–1494.
- Rice, G.I. et al, (2012). Mutations in ADAR1 cause Aicardi-Goutières syndrome associated with a type i interferon signature. *Nature Genet.* 44, 1243–1248.
- 8. Livingston, J.H. et al, (2014). A type i interferon signature identifies bilateral striatal necrosis due to mutations in ADAR1. *J. Med. Genet.* **51**, 76–82.
- 9. Herbert, A., (2020). Mendelian disease caused by variants affecting recognition of Z-DNA and Z-RNA by the $Z\alpha$ domain of the double-stranded RNA editing enzyme ADAR. *Eur. J. Hum. Genet.* **28**, 114–117.
- Heraud-Farlow, J.E., Walkley, C.R., (2020). What do editors do? Understanding the physiological functions of A-to-I RNA editing by adenosine deaminase acting on RNAs: In vivo functions of A-to-I RNA editing. Open Biol. 10
- Rice, G. et al, (2007). Clinical and molecular phenotype of Aicardi-Goutières syndrome. Am. J. Hum. Genet. 81, 713– 725.
- Aniello, M.S. et al, (2008). Bilateral striatal necrosis, dystonia and multiple mitochondrial DNA deletions: Case study and effect of deep brain stimulation. *Mov. Disord.* 23, 114–118.
- Daou, S. et al, (2020). A phenolic small molecule inhibitor of RNase L prevents cell death from ADAR1 deficiency. *Proc. Natl. Acad. Sci. U. S. A.* 117, 24802–24812.
- Schwartz, T., Rould, M.A., Lowenhaupt, K., Herbert, A., Rich, A., (1999). Crystal structure of the Zα domain of the human editing enzyme ADAR1 bound to left-handed Z-DNA. *Science* (80-.) 284, 1841–1845.
- 15. Placido, D., Brown, B.A., Lowenhaupt, K., Rich, A., Athanasiadis, A., (2007). A Left-Handed RNA Double Helix Bound by the $Z\alpha$ Domain of the RNA-Editing Enzyme ADAR1. *Structure* 15, 395–404.
- 16. Van Quyen, D. et al, (2007). Characterization of DNA-binding activity of $Z\alpha$ domains from poxviruses and the importance of the β -wing regions in converting B-DNA to Z-DNA. *Nucleic Acids Res.* **35**, 7714–7720.
- Nakahama, T. et al, (2021). Mutations in the adenosine deaminase ADAR1 that prevent endogenous Z-RNA binding induce Aicardi-Goutières-syndrome-like encephalopathy. *Immunity* 54, 1976–1988.e7.
- Feng, S. et al, (2011). Alternate rRNA secondary structures as regulators of translation. *Nature Struct. Mol. Biol.* 18, 169–177.
- 19. Jeong, M. et al, (2014). NMR study of the Z-DNA binding mode and B-Z transition activity of the $Z\alpha$ domain of human ADAR1 when perturbed by mutation on the α 3 helix and β -hairpin. *Arch. Biochem. Biophys.* **558**, 95–103.
- Vögeli, B., Güntert, P., Riek, R., (2013). Multiple-state ensemble structure determination from eNOE spectroscopy. *Mol. Phys.* 111, 437–454.

- Nichols, P.J. et al, (2020). Reducing the measurement time of exact NOEs by non-uniform sampling. *J. Biomol. NMR* 74, 717–739.
- 22. Beyer, U. et al, (2017). Rare ADAR and RNASEH2B variants and a type I interferon signature in glioma and prostate carcinoma risk and tumorigenesis. *Acta Neuropathol.* 134, 905–922.
- Lee, A.R. et al, (2016). Solution structure of the Z-DNA binding domain of PKR-like protein kinase from Carassius auratus and quantitative analyses of the intermediate complex during B-Z transition. *Nucleic Acids Res.* 44, 2936–2948.
- Faber, H.R., Matthews, B.W., (1990). A mutant T4 lysozyme displays five different crystal conformations. Nature 348, 263–266.
- 25. Buel, G.R., Walters, K.J., (2022). Can AlphaFold2 predict the impact of missense mutations on structure? *Nature Struct. Mol. Biol.* 29, 1–2.
- Mirdita, M. et al, (2022). ColabFold: making protein folding accessible to all. Nature Methods 19, 679–682.
- Hyberts, S.G., Milbradt, A.G., Wagner, A.B., Arthanari, H., Wagner, G., (2012). Application of Iterative Soft Thresholding for Fast Reconstruction of NMR Data Nonuniformly Sampled with Multidimensional Poisson Gap Scheduling. J Biomol NMR 52, 315–327.
- Schade, M. et al, (1999). The solution structure of the Za domain of the human RNA editing enzyme ADAR1 reveals a prepositioned binding surface for Z-DNA. *Proc. Natl. Acad. Sci. U. S. A.* 96, 12465–12470.

- Nichols, P.J., Henen, M.A., Vicens, Q., Vögeli, B., (2021). Solution NMR backbone assignments of the N-terminal Zα-linker-Zβ segment from Homo sapiens ADAR1p150. Biomol. NMR Assign. 15, 273–279.
- Liu, Y., Prestegard, J.H., (2008). Direct measurement of dipole-dipole/CSA cross-correlated relaxation by a constant-time experiment. J Magn Reson. 193, 23–31.
- Delaglio, F. et al, (1995). NMRPipe: A multidimensional spectral processing system based on UNIX pipes. J. Biomol. NMR 6, 277–293.
- Vranken, W.F. et al, (2005). The CCPN data model for NMR spectroscopy: Development of a software pipeline. Proteins Struct. Funct. Genet. 59, 687–696.
- Kay, L.E., Torchia, D.A., Bax, A., (1989). Backbone Dynamics of Proteins As Studied by 15N Inverse Detected Heteronuclear NMR Spectroscopy: Application to Staphylococcal Nuclease. *Biochemistry* 28, 8972– 8979.
- **34.** Orts, J., Vögeli, B., Riek, R., (2012). Relaxation matrix analysis of spin diffusion for the NMR structure calculation with eNOEs. *J. Chem. Theory Comput.* **8**, 3483–3492.
- 35. Güntert, P., Buchner, L., (2015). Combined automated NOE assignment and structure calculation with CYANA. *J. Biomol. NMR* 62, 453–471.
- Strotz, D., Orts, J., Chi, C.N., Riek, R., Vögeli, B., (2017).
 ENORA2 Exact NOE Analysis Program. J. Chem. Theory Comput. 13, 4336–4346.

Supplemental Materials:

Differential Structural Features of Two Mutant ADAR1p150 Zα Domains Cause Aicardi-Goutières Syndrome

Conner J. Langeberg¹, Parker J. Nichols¹, Morkos A. Henen^{1,2}, Quentin Vicens^{1,3*} and Beat Vögeli^{1,3*}

Contents:

Figure S1: 15 N-HSQC spectra of $Z\alpha_{WT}$ and $Z\alpha_{N173S}$ Figure S2: 15 N-HSQC spectra of $Z\alpha_{WT}$ and $Z\alpha_{P193A}$

Figure S3: R₁ relaxation rates of mutant Zα

Figure S4: Cross-correlated relaxation rates of mutant Zα

Figure S5: $R_{1\rho}$ relaxation rates of mutant $Z\alpha$

Figure S6: eNOE map of mutant $Z\alpha$ **Figure S7:** Comparison of $Z\alpha$ domains

Figure S8: Comparison of mutant Zα domains to AlphaFold2 predicted structures

Table S1: Experimental restraints and structural statistics of mutant Za

¹Department of Biochemistry and Molecular Genetics and ³RNA Bioscience Initiative, University of Colorado Denver School of Medicine, Aurora, Colorado, 80045, USA.

²Faculty of Pharmacy, Mansoura University, Mansoura 35516, Egypt.

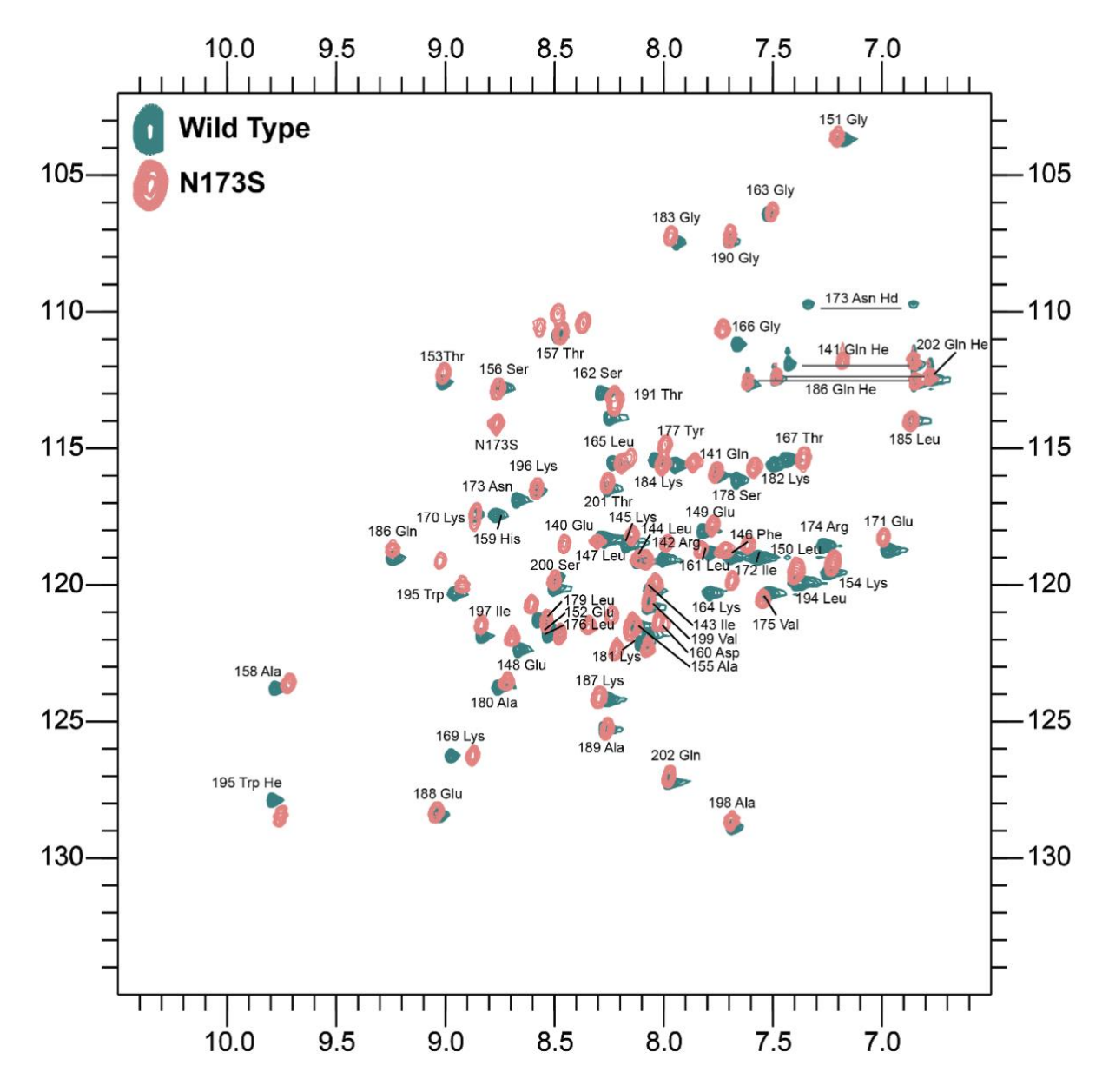


Fig. S1: The superposition of the 15 N-HSQC (heteronuclear single-quantum correlation) spectra of $Z\alpha_{WT}$ (green) and $Z\alpha_{N173S}$ (pink).

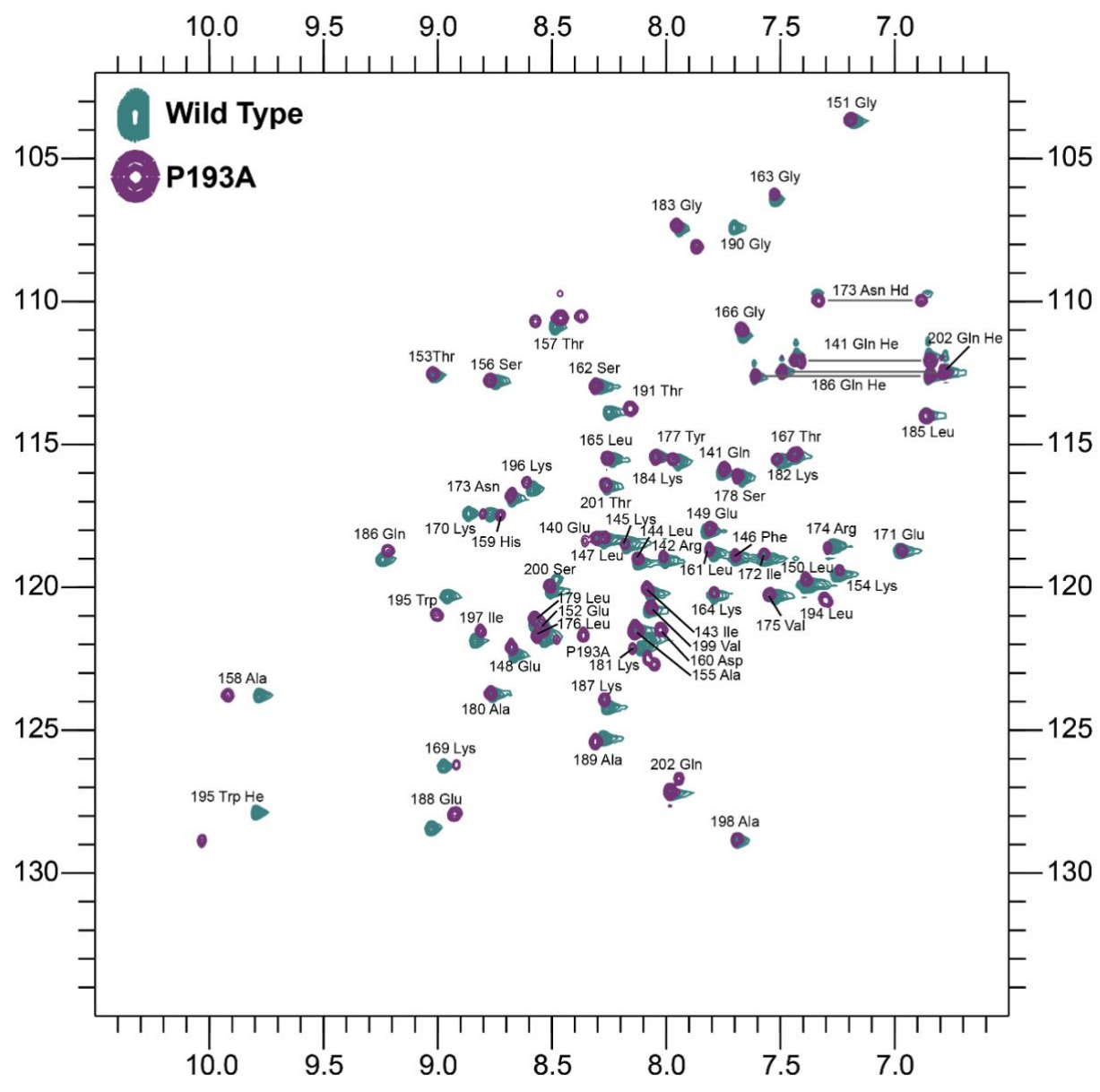


Fig. S2: The superposition of the 15 N-HSQC (heteronuclear single-quantum correlation) spectra of $Z\alpha_{WT}$ (green) and $Z\alpha_{P193A}$ (purple).

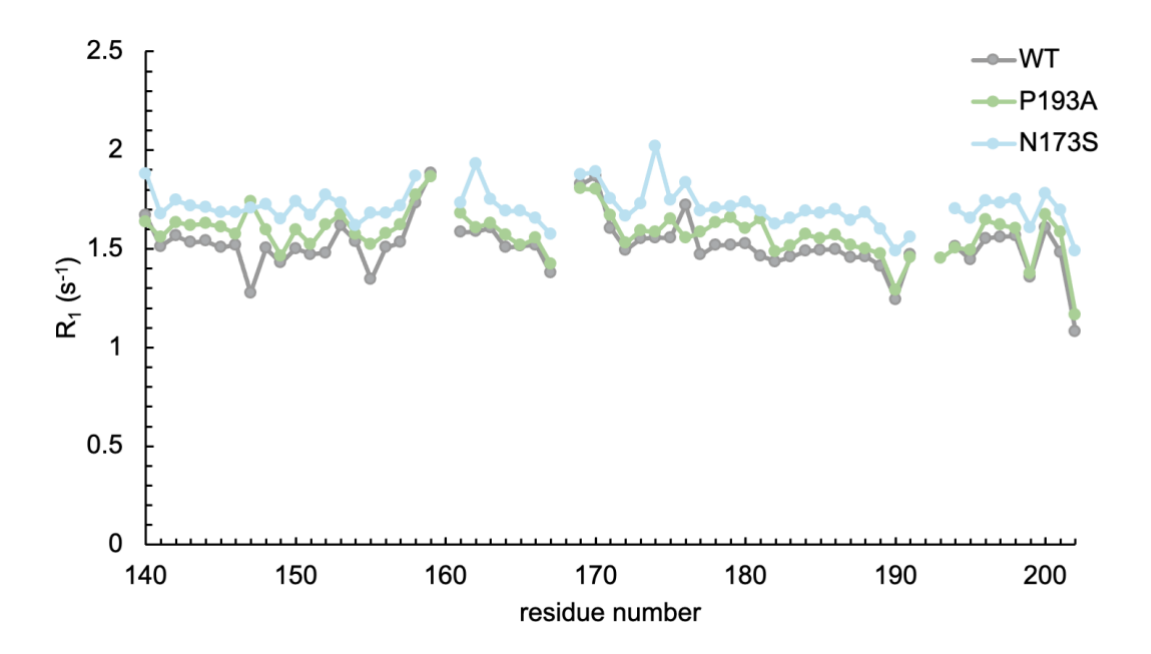


Fig. S3: 15 N-R₁ relaxation rates of Z α_{WT} (grey), Z α_{N173S} (green), and Z α_{P193A} (blue).

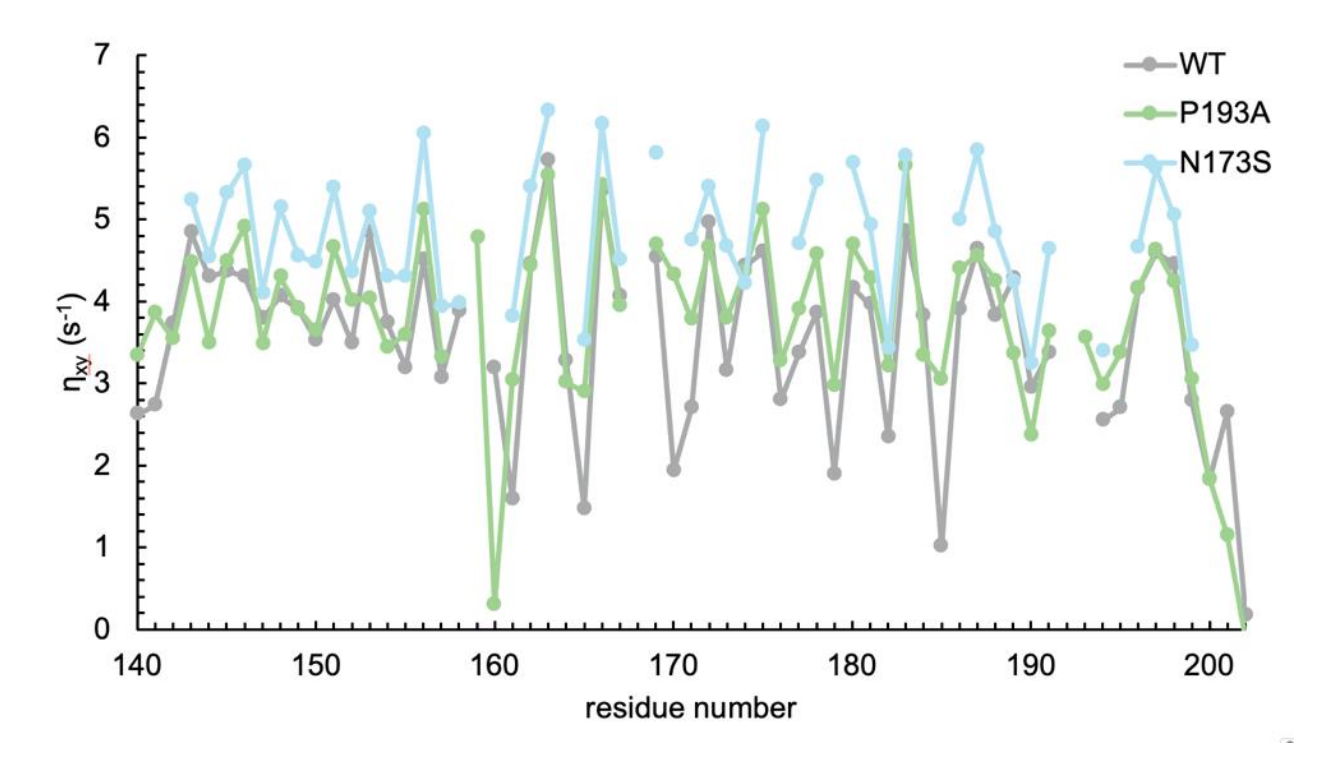


Fig. S4: ^{15}N - ^{1}H -dipole/ ^{15}N -CSA cross-correlated relaxation rates (η_{xy}) of $Z\alpha_{WT}$ (grey), $Z\alpha_{N173S}$ (green), and $Z\alpha_{P193A}$ (blue).

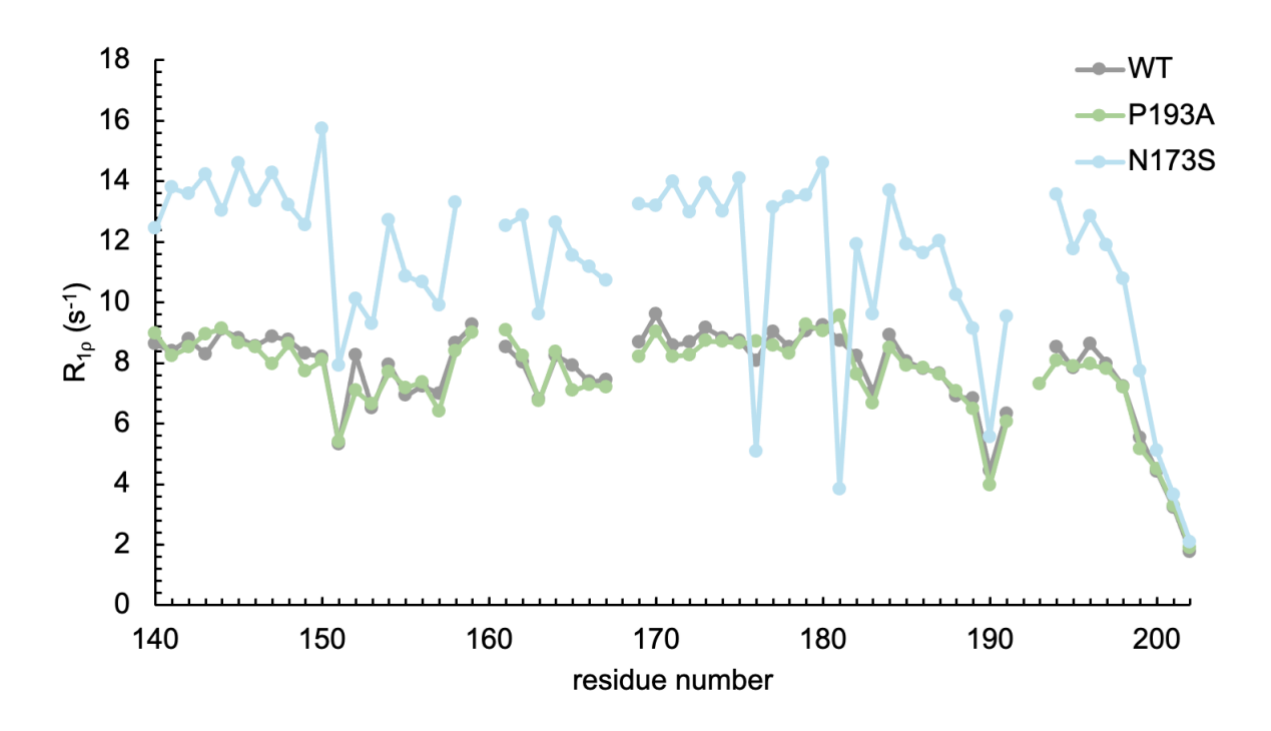


Fig. S5: $^{15}N-R_{1\rho}$ relaxation rates of $Z\alpha_{WT}$ (grey), $Z\alpha_{N173S}$ (green), and $Z\alpha_{P193A}$ (blue).

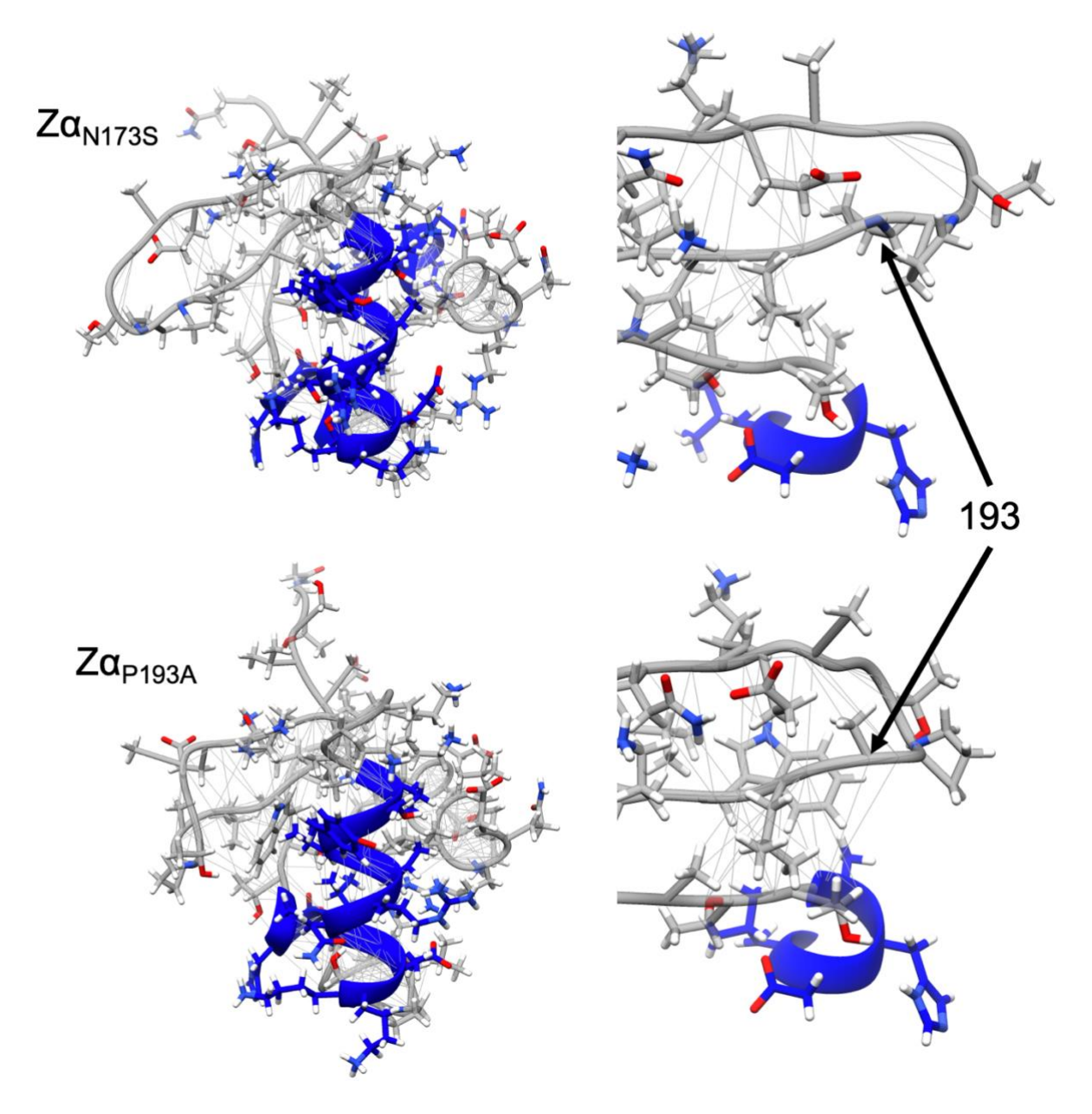


Fig. S6: Representative solution state structure of $Z\alpha_{N173S}$ (top left), and $Z\alpha_{P193A}$ (bottom left), and beta-wing region of $Z\alpha_{N173S}$ (top right), and $Z\alpha_{P193A}$ (bottom right), with applied eNOE restraints mapped onto the structure.

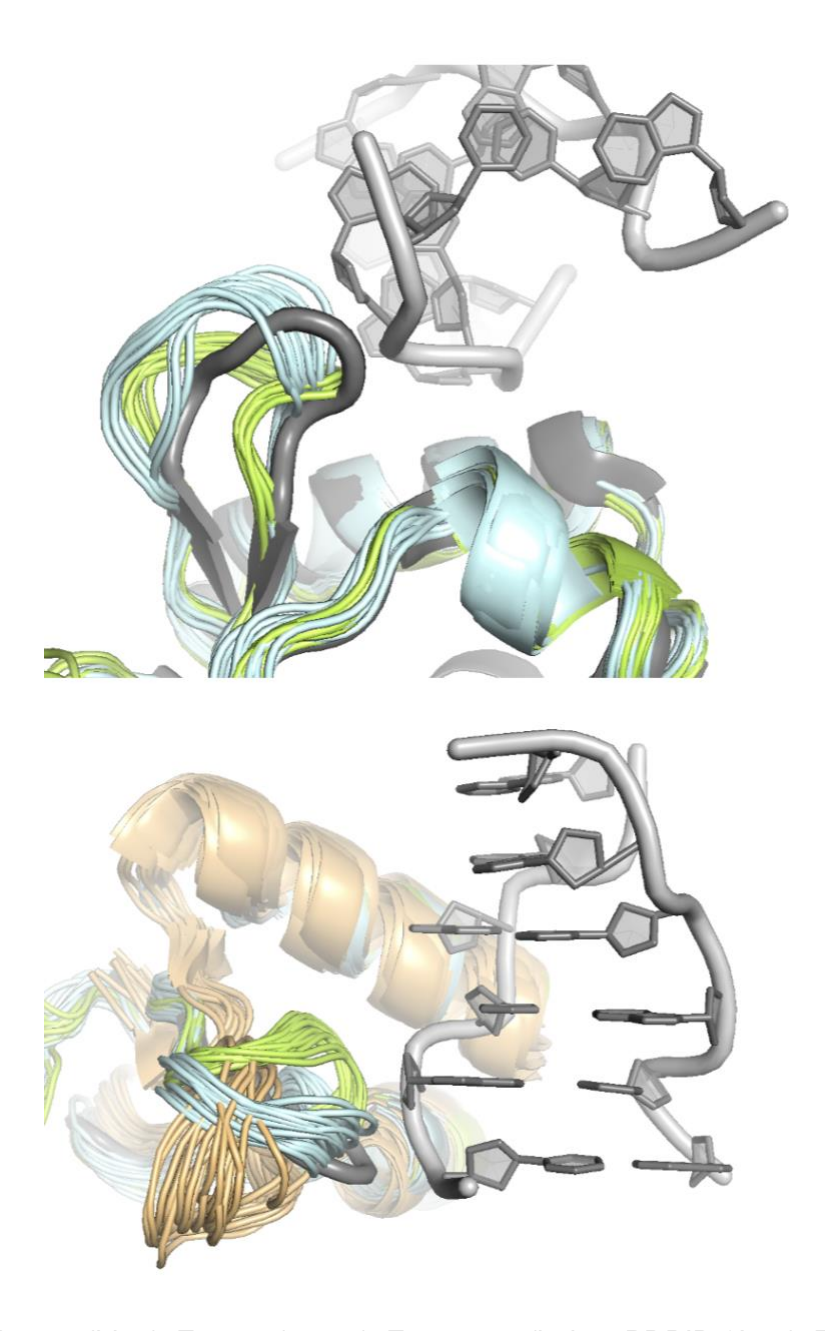


Fig. S7: Overlay of $Z\alpha_{N173S}$ (blue), $Z\alpha_{P193A}$ (green), $Z\alpha_{N43A,Y47A}$ (beige, PDBID:2L54), $Z\alpha_{WT}$ (grey, PBDID: 1QBJ) showing beta-wing positioning across the structures determined here and previously determined structures.

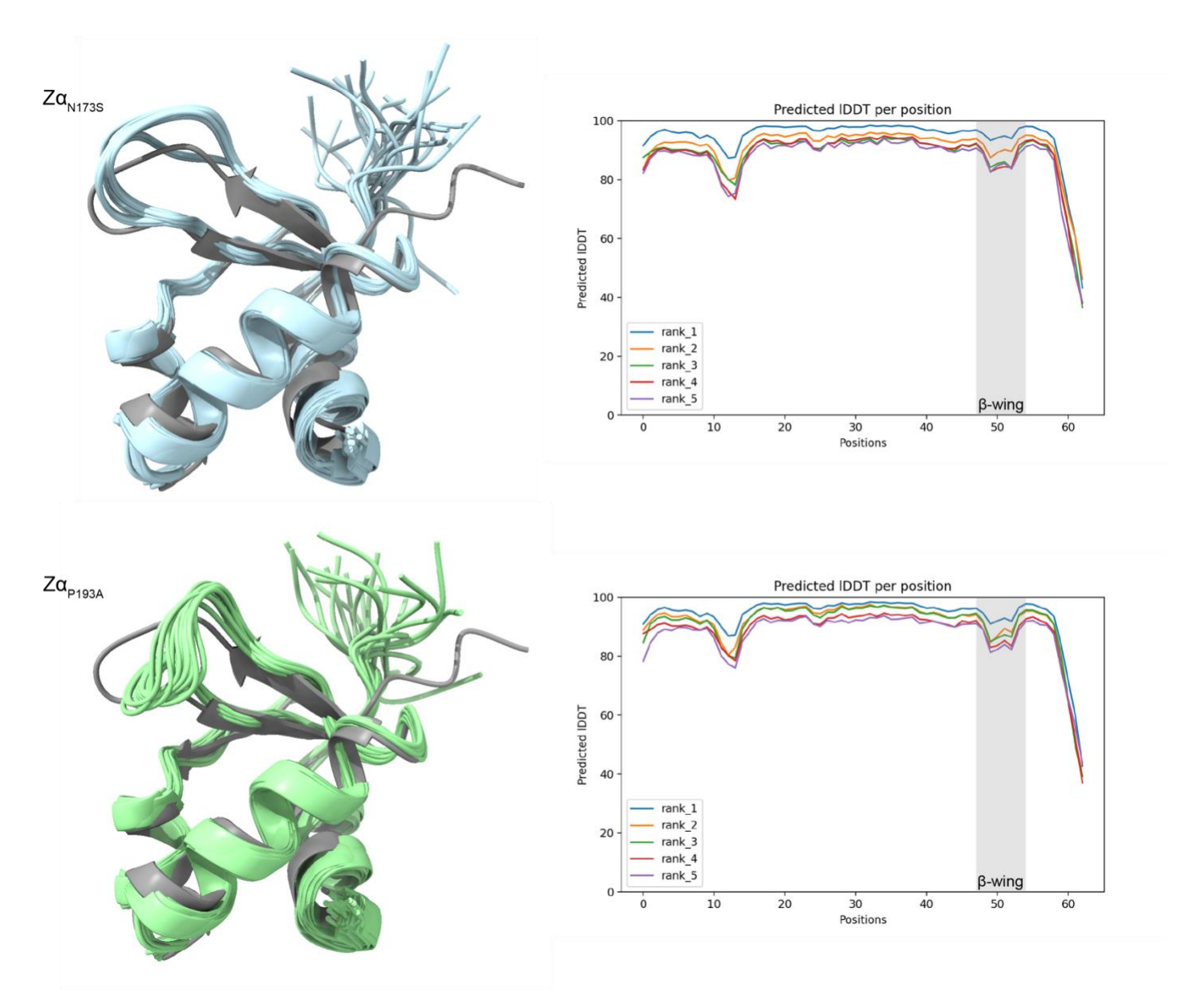


Fig. S8: Overlay of $Z\alpha_{N173S}$ (blue, top left), $Z\alpha_{P193A}$ (green, bottom left) with models generated using AlphaFold2 showing its inability to recapitulate structural perturbations resulting from the single residue mutations. Predicted IDDT score of top 5 predicted structures of $Z\alpha_{N173S}$ (blue, top left) and $Z\alpha_{P193A}$ (green, bottom left) with the beta wing highlighted.

NMR distance and angle constraints	$Z\alpha_{N173S}$	Zα _{P193A}
Distance constraints		
Total eNOE	711	764
Intraresidue	138	144
Interresidue		
Sequential (i-j =1)	99	101
Medium range (1< i-j <5)	315	331
Long range (i-j >3)	159	188
Total dihedral angle restraints		
ф	53	54
Ψ	54	55
Structure statistics		
Violations (mean and SD)		
Distance constraints (Å)	1.38±0.02	1.51±0.10
Dihedral angle constraints (°)	14.5±0.75	17.4±1.62
Max. dihedral angle violation (°)	15.7	20.0
Max. distance constraint violation (Å)	1.43	1.63
Deviation from idealized geometry		
Bond lengths (Å)	0.001	0.001
Bond angles (°)	0.2	0.2
Average pairwise r.m.s. deviation backbone (20 structures) (Å)	1.0	1.1
Average pairwise r.m.s. deviation heavy atom (20 structures) (Å)	1.7	1.7
Ramachandran plot, % residues		
Most favored regions	83.4%	78.4%
Additional allowed regions	15.5%	20.0%
Generously allowed regions	1.1%	1.6%
Disallowed regions	0.0%	0.0%

Table S1: Experimental restraints and structural statistics.